Geology

Uncovering framboidal pyrite biogenicity using nano-scale CNorg mapping

--Manuscript Draft--

Manuscript Number:	G36048R1
Full Title:	Uncovering framboidal pyrite biogenicity using nano-scale CNorg mapping
Short Title:	Framboidal pyrite
Article Type:	Article
Keywords:	pyrite; framboids; sulfur isotopes; biomarker; biofilms
Corresponding Author:	David Wacey The University of Western Australia Perth, Western Australia AUSTRALIA
Corresponding Author Secondary Information:	
Corresponding Author's Institution:	The University of Western Australia
Corresponding Author's Secondary Institution:	
First Author:	David Wacey
First Author Secondary Information:	
Order of Authors:	David Wacey
	Matt R Kilburn
	Martin Saunders
	John B Cliff
	Charlie Kong
	Alexander G Liu
	Jack J Matthews
	Martin D Brasier
Order of Authors Secondary Information:	
Manuscript Region of Origin:	CANADA
Abstract:	Framboidal pyrite has been used as a paleo-redox proxy and a biomarker in ancient sediments, but the interpretation of pyrite framboids can be controversial, especially where later overgrowths have obscured primary textures. Here we show how nano-scale chemical mapping of organic carbon and nitrogen (CNorg) can detect relict framboids within Precambrian pyrite grains and determine their formation mechanism. Pyrite grains associated with Ediacaran fossil lagerstätten from Newfoundland (c. 560 Ma) hold significance for our understanding of taphonomy and redox history of the earliest macrofossil assemblages. They show distinct chemical zoning with respect to CNorg. Relict framboids are revealed as spheroidal zones within larger pyrite grains, whereby pure pyrite micro-crystals are enclosed by a mesh-like matrix of pyrite possessing elevated CNorg, replicating observations from framboids growing within modern biofilms. Subsequent pyrite overgrowths also incorporated CNorg from biofilms, with concentric CNorg zoning showing that the availability of CNorg progressively decreased during later pyrite growth. Multiple framboids are often cemented together by these overgrowths to form larger grains, with relict framboids only detectable in CNorg maps. In situ sulfur isotope data (δ34S = c. −24 ‰ to −15 ‰) show that the source of sulfur for the pyrite was also biologically mediated, most likely via a sulfate-reducing microbial metabolism within the biofilms. Relict framboids have significantly smaller diameters than the pyrite grains that enclose them, suggesting that the use of framboid diameters to infer water column paleo-redox conditions should be

	approached with caution. This work shows that pyrite framboids have formed within organic biofilms for at least 560 Ma, and provides a novel methodology that could readily be extended to search for such biomarkers in older rocks and potentially on other planets.
Response to Reviewers:	All responses are given in the attached cover letter

Publisher: GSA
Journal: GEOL: Geology
DOI:10.1130/G36048.1

Uncovering framboidal pyrite biogenicity using nano-scale CN_{org} mapping

David Wacey[1,2], Matt R. Kilburn[1,2], Martin Saunders[2], John B. Cliff[1,2], Charlie Kong[3], Alexander G. Liu[4], Jack J. Matthews[5], and Martin D. Brasier[5]

[1]*Australian Research Council Centre of Excellence for Core to Crust Fluid Systems, The University of Western Australia, 35 Stirling Highway, Crawley, WA 6009, Australia*

[2]*Centre for Microscopy Characterisation and Analysis, The University of Western Australia, 35 Stirling Highway, Crawley, WA 6009, Australia*

[3]*Electron Microscopy Unit, University of New South Wales, Kingsford, NSW 2052, Australia*

[4]*Department of Earth Sciences, University of Cambridge, Downing Street, Cambridge, CB2 3EQ, UK*

[5]*Department of Earth Sciences, University of Oxford, South Parks Road, Oxford, OX1 3AN, UK*

ABSTRACT

Framboidal pyrite has been used as a paleo-redox proxy and a biomarker in ancient sediments, but the interpretation of pyrite framboids can be controversial, especially where later overgrowths have obscured primary textures. Here we show how nano-scale chemical mapping of organic carbon and nitrogen (CN_{org}) can detect relict framboids within Precambrian pyrite grains and determine their formation mechanism.

Pyrite grains associated with Ediacaran fossil lagerstätten from Newfoundland (c. 560 Ma) hold significance for our understanding of taphonomy and redox history

Publisher: GSA
Journal: GEOL: Geology
DOI:10.1130/G36048.1

of the earliest macrofossil assemblages. They show distinct chemical zoning with respect to CN_{org}. Relict framboids are revealed as spheroidal zones within larger pyrite grains, whereby pure pyrite micro-crystals are enclosed by a mesh-like matrix of pyrite possessing elevated CN_{org}, replicating observations from framboids growing within modern biofilms. Subsequent pyrite overgrowths also incorporated CN_{org} from biofilms, with concentric CN_{org} zoning showing that the availability of CN_{org} progressively decreased during later pyrite growth. Multiple framboids are often cemented together by these overgrowths to form larger grains, with relict framboids only detectable in CN_{org} maps. In situ sulfur isotope data ($\delta^{34}S$ = c. –24 ‰ to –15 ‰) show that the source of sulfur for the pyrite was also biologically mediated, most likely via a sulfate-reducing microbial metabolism within the biofilms. Relict framboids have significantly smaller diameters than the pyrite grains that enclose them, suggesting that the use of framboid diameters to infer water column paleo-redox conditions should be approached with caution.

This work shows that pyrite framboids have formed within organic biofilms for at least 560 Ma, and provides a novel methodology that could readily be extended to search for such biomarkers in older rocks and potentially on other planets.

INTRODUCTION

Framboidal pyrite is a common component of the geological record, often being the most common pyrite texture in ancient sediments, but its formation mechanism has long been debated (Papunen, 1966; Ohfuji and Rickard, 2005; Ohfuji et al., 2005; Rickard, 2012). Pyrite framboids are defined as microscopic spheroidal to sub-spheroidal clusters of equidimensional and equimorphic pyrite microcrystals (Ohfuji and Rickard, 2005). A single framboid may contain up to 10^6 approximately cubic or octahedral pyrite micro-crystals, and may be 1–250 μm across (Ohfuji and

Publisher: GSA
Journal: GEOL: Geology
DOI:10.1130/G36048.1

Rickard, 2005), although they are most commonly 10–20 μm in diameter (Wilkin et al., 1996; Wang et al., 2012). Pyrite framboids have been used as a proxy for local redox conditions in paleo-environmental reconstructions, with their size distributions used to discriminate between formation within euxinic water columns or in sediments below oxygenated water columns (Wilkin et al., 1996; Wang et al., 2012). They have also been suggested as potential biomarkers in very ancient sediments or on other planets (Popa et al., 2004; MacLean et al., 2008). Hence, there is a pressing need for robust ways to identify framboids, accurately measure their size distributions, and determine their biogenicity throughout the geological record.

Early studies noted a frequent association of organic matter with pyrite framboids, leading to the suggestion that their characteristic texture was directly controlled by biology, with some studies speculating that framboids were pyritised microfossils (e.g., Love, 1957). However, the discovery of framboids in high temperature volcanic and hydrothermal settings (Love and Amstutz, 1969), plus the experimental synthesis of pyrite framboids in the laboratory without the presence of organic material (Sweeney and Kaplan, 1973), indicated that biology was not a pre-requisite for framboid formation. Substantial debate followed about the extent to which biology contributes to framboid formation (e.g., Ohfuji and Rickard, 2005; Kohn et al., 1998). In modern low temperature sedimentary environments, much of this debate was resolved by the work of Large et al. (2001) and MacLean et al. (2008). These authors used high-spatial-resolution cryogenic-SEM (Large et al., 2001), plus focused ion beam-SEM and X-ray spectroscopy (MacLean et al., 2008) to demonstrate the presence of biofilms coating both the outer surface of complete pyrite framboids and the surfaces of individual micro-crystals within a framboid. Partially formed ‘proto-framboids’ were found to be embedded in particularly large quantities

Publisher: GSA
Journal: GEOL: Geology
DOI:10.1130/G36048.1

of biofilm and possessed micro-crystals with anhedral crystal faces, suggesting that biofilms provide an organic template (constrained growth space) for the growth and aggregation of pyrite micro-crystals (MacLean et al., 2008). Furthermore, the polysaccharide-dominated surfaces of biofilms have a strong affinity for Fe^{2+} ions, providing ideal nucleation sites for iron sulfides, and may also play a role in stabilizing the framboids during sediment compaction or disturbance (Large et al., 2001).

In ancient environments, however, where significant pyrite recrystallization may have taken place and framboid-containing rocks may have experienced both low temperature and high temperature conditions (cf. Scott et al., 2009), it is more difficult to securely identify pyrite framboids and to demonstrate a biological formation mechanism. Some ancient framboids still retain their characteristic morphology when viewed under reflected light or the SEM but many others, such as those studied here, may be 'hidden' within larger grains. Chemical etching may hint at hidden framboids (Rickard and Zweifel, 1975) and $\delta^{34}S$ data may indicate whether the sulfur incorporated into framboids has a biogenic source (Kohn et al., 1998), but these data do not reveal whether framboid growth occurred within a biological matrix. Furthermore, the small size of framboids means that conventional bulk isotopic and elemental analyses lack the spatial resolution required to provide meaningful data. Here we combine in situ secondary ion mass spectrometry (SIMS) and transmission electron microscopy (TEM) to provide a new way to detect and measure relict framboids within ancient pyrite grains, and evaluate the contribution of biology to their nucleation and growth mechanisms.

METHODS

Publisher: GSA
Journal: GEOL: Geology
DOI:10.1130/G36048.1

Ion mapping was performed on portions of standard geological thin sections using a *CAMECA NanoSIMS 50*, with instrument parameters optimized as described in Wacey et al. (2011). TEM wafers were extracted from geological thin sections using a *FEI xT Nova NanoLab 200* focused ion beam-scanning electron microscope, and TEM data were obtained using a *FEI Titan G2 80-200* TEM/STEM with *ChemiSTEM Technology*, plus a *JEOL 2100* LaB_6 TEM. Sulfur isotope data were obtained using a *CAMECA NanoSIMS 50* and a *CAMECA IMS 1280*, following protocols described in McLoughlin et al. (2012) and Farquhar et al. (2013) respectively. For detailed methods see GSA Data Repository item 2014xxx.

RESULTS AND DISCUSSION

Pyrite Chemistry and Nanotexture

Turbiditic siltstones of the ~560 Ma Fermeuse Formation at Back Cove, Bonavista Peninsula, Newfoundland, contain clusters and laminae of small (<50 μm) pyrite grains (Fig. DR1). Pyrite morphology ranges from rounded, through to subhedral and euhedral cubes. Secondary electron (SE) images and NanoSIMS sulfur ($^{34}S^-$) ion maps show no indication of framboidal morphologies; indeed they indicate a rather homogenous textural and chemical composition for all pyrite grains (Figs. 1, 2c), with no significant differences between small rounded grains and larger euhedral grains (compare $^{34}S^-$ images of small rounded grain at top of Figure 1 with large grain in Fig. 2). In contrast, carbon ($^{12}C^-$) and nitrogen ($^{26}CN^-$) NanoSIMS ion maps reveal distinct nano-scale chemical zoning within and between these grains. Many pyrite grains possess an inner spheroidal zone (ISZ; Figure 1, dashed circle in enlarged $^{26}CN^-$ map) comprising numerous micro-crystals of pure pyrite (Fig. 1, black cuboids in enlarged $^{26}CN^-$ map) set within a mesh-like matrix of C- and N-rich pyrite (Fig. 1, pink areas within dashed circle in $^{26}CN^-$ map). The ISZ is usually surrounded by an

Publisher: GSA
Journal: GEOL: Geology
DOI:10.1130/G36048.1

outer zone (OZ) of C- and N-rich pyrite (Fig. 1, outer blue and pink zones). Co-occurrence of C and N, combined with the absence of ions such as Ca or O, indicates that the C and N signals come from organic material preserved within the pyrite grains (from now on referred to as CN_{org}).

TEM images of ultrathin (c.100 nm) cross sections through well-preserved grains demonstrate the nano-texture of the ISZ and the OZ, and also show that the grains have a distinct thin (<500 nm) outer rim (Fig. 2d-e). In the ISZ, pyrite micro-crystals are close packed, as expected for framboidal pyrite (cf. Ohfuji and Rickard, 2005), and each of these pyrite micro-crystals has a thin (c.50–100 nm) nano-porous rim (Fig. 2d-e, arrows). The OZ also has a nano-porous texture and these pores tend to be slightly larger than those in the ISZ (Fig. 2c). The nano-porous rims of the ISZ together with the nano-porous OZ correspond precisely to the areas of CN_{org} enrichment seen in NanoSIMS ion maps. Unfortunately, the relatively poor detection limits for N, together with the extreme thinness of the TEM sample, preclude accurate mapping of CN_{org} in the TEM. Only relatively large clumps of CN_{org} at some crystal boundaries can be visualized in the TEM (Fig. DR2). We suggest that the nano-pores house the remaining CN_{org} seen in NanoSIMS maps, but it is also possible that CN_{org} is held within the pyrite crystal lattice itself in these areas. Arsenic and nickel occur in trace amounts restricted to the nano-porous rims of the ISZ (and to a lesser amount in the OZ), correlating with the CN_{org} enrichment seen in the NanoSIMS maps (Fig. DR2). At the boundary between the ISZ and the OZ, the ISZ micro-crystals are sharply terminated against the OZ (Fig. 2d, white line) and are not equimorphic with micro-crystals toward the center of the ISZ. This suggests either recrystallization of outer portions of the ISZ to form the OZ or a fairly rapid change in local chemistry, such as reduction of free iron concentration, that changed pyrite growth morphology.

The thin outer rim records minor late-stage oxidation of pyrite to iron oxide (Fig. DR3).

Some single pyrite grains possess several ISZ separated and surrounded by OZ pyrite (Fig. 2a-b; Fig. DR4). In these cases, the grains often exhibit a rather euhedral shape that disguises their original formation mechanism (Fig. 2). In other examples, the OZ is chemically heterogenous in CN_{org}, with clear concentric zoning marked by outward-decreasing CN_{org} contents (Fig. DR5). Occasionally the CN_{org} chemical microstructure of the ISZ is completely lost and only a spheroid of pure pyrite is seen (Fig. DR6).

We interpret the ISZ in these grains as relict primary pyrite framboids and the OZ as secondary pyrite. For those pyrite grains that possess several ISZ, these are interpreted as multiple, closely spaced relict primary framboids that were cemented together by secondary pyrite overgrowths. The distribution of CN_{org} in most ISZ closely resembles the pattern of organic enrichment seen in modern framboidal pyrite that nucleated and grew within biofilms (Large et al., 2001). The nano-texture of the ISZ is also near identical to that seen in modern biologically-mediated framboids, where every pyrite micro-crystal in the framboid is enclosed by a thin biofilm (compare Figure 2d-e with fig. 2c of MacLean et al., 2008). Hence, we conclude that our 560 Ma framboids likewise nucleated and grew within biofilms, or within some other organic material such as extra-cellular polymeric substances (EPS). Wispy carbonaceous laminae observed in thin sections close to the framboid-bearing layer (Fig. DR1a) likely represent the remains of biofilms. Biofilms provide a number of favorable conditions for framboid formation: 1) the organic framework provides a pre-existing confined growth space that can control crystal size and morphology (MacLean et al., 2008); 2) biofilms replicate conditions of high Fe and S

Publisher: GSA
Journal: GEOL: Geology
DOI:10.1130/G36048.1

supersaturation (required for successful experimental abiotic precipitation of pyrite framboids; Ohfuji and Rickard, 2005) so that nucleation rate is significantly greater than crystal growth rate; 3) biofilms contain large amounts of polysaccharides that have a high Fe^{2+} binding capacity, enhancing crystal nucleation (Flemming, 1995; likewise, Ni and As could also be preferentially bound by biofilms, consistent with their enrichment in CN_{org} zones); 4) cell walls within biofilms provide further preferred nucleation sites for metal sulfides (Ferris et al., 1987); and 5) metal-reducing and sulfate-reducing bacteria in biofilms can provide a local source of reactive iron and sulfide (Rickard, 2012). In modern framboids, a layer of biofilm also tends to enclose the entire framboid (Large et al., 2001; MacLean et al., 2008). While this could equate to the OZ observed in our pyrite grains, our OZ are much thicker than modern biofilm coatings. This, together with our nano-textural observations above, suggests the OZ is instead a zone of secondary overgrowth and/or recrystallisation.

Insights from Sulfur Isotope Geochemistry

Sulfur isotope data (Table DR1; Fig. 3) were obtained in situ from polished geological thin sections using *Cameca NanoSIMS 50* and *Cameca IMS 1280* ion probes. Pyrite grains show a uniformly light $\delta^{34}S$ signal (–15.2 ‰ to –24.3 ‰; mean = –21.5 ‰; n = 33). There is no significant difference in data obtained using NanoSIMS (mean = –21.7 ‰) and IMS 1280 (mean = –21.4 ‰).

This spatially resolved $\delta^{34}S$ data informs on the source of the sulfur for the pyrite. Taking $\delta^{34}S$ = +25 ‰ as a mean estimate for the isotopic composition of seawater sulfate at this time (Fike et al., 2006), then the pyrite grains show maximum fractionations from Ediacaran seawater sulfate ($\Delta\delta^{34}S$) of almost 50 ‰ ($\Delta\delta^{34}S$ = 40.2–49.3 ‰). This clearly shows biological processing of sulfur prior to incorporation into

Publisher: GSA
Journal: GEOL: Geology
DOI:10.1130/G36048.1

the pyrite. Such large $\Delta\delta^{34}S$ fractionations may occur in two ways: 1) during microbial sulfate reduction (MSR) under conditions of limited electron donor supply and/or poor reactivity of organic material (Leavitt et al., 2013); and 2) during oxidative sulfur cycling where fractionations associated with MSR are supplemented by those occurring during disproportionation of oxidized sulfide (Canfield and Thamdrup, 1994). We favor the former mechanism here due to the inferred deep-sea setting (Hofmann et al., 2008), leading to low C_{org} delivery and relatively low total organic carbon (TOC) contents of these sediments (mostly < 0.1 wt%; Canfield et al., 2007). Although microbial biomorphs have not yet been observed in the pyrite grains, it is likely that sulfate-reducing bacteria were part of the living biofilm in which the framboids nucleated and grew, producing a localized source of ^{34}S-depleted H_2S for incorporation into the pyrite micro-crystals.

$\delta^{34}S$ does not change significantly with distance from the center of a pyrite grain (Fig. 3). This supports our earlier hypothesis that pyrite overgrowths could have resulted from recrystallization of primary framboidal zones (hence inheriting their isotopic signal). This mechanism is also consistent with the homogenous enrichment of CN_{org} in the overgrowths of many grains; here, CN_{org} that was present in biofilms coating framboid micro-crystals could be redistributed and incorporated into nano-pores or the crystal lattice of pyrite as it recrystallized. For those grains with concentrically zoned and outward-diminishing CN_{org} contents (e.g., Fig. DR5), we infer that recrystallization was followed by continued early diagenetic pyrite growth in pore-waters that were CN_{org} poor but were still open to a supply of iron and seawater sulfate (hence, no Rayleigh-type ^{34}S enrichment in the $\delta^{34}S$ data).

Implications for the use of Framboid Diameters as a Paleo-redox Proxy

Publisher: GSA
Journal: GEOL: Geology
DOI:10.1130/G36048.1

Framboid diameters have been used to determine whether pyrite precipitation took place within a euxinic water column or within sediments below an oxic or dysoxic water column (e.g., Wilkin et al., 1996; Wang et al., 2012). In modern environments, framboids precipitated within a euxinic water column over a short timespan tend to be <10 μm in diameter, whereas those precipitated in sediment porewaters have larger and more variable diameters (Wilkin et al., 1996). This protocol has been extended into the geological record and used to infer the oxidation state of some ancient water columns (Wang et al., 2012). However, when we compare the diameters of the relict framboids (defined as the ISZ in the NanoSIMS CN_{org} maps) with the total diameter of the enclosing grains, we find that the relict framboids make up only 15% to 71% of total grain diameter (n=28). Moreover, several enclosing grains retain a spheroidal, pseudo-framboidal shape despite clearly not being primary framboids. These data suggest simple transects using light or electron microscopy are insufficient to determine the portion of a framboid that is primary in nature and hence extreme caution should be exercised if attempting to use framboid diameters as paleo-redox proxies.

CONCLUSION

Pyrite grains from 560 Ma sediments exhibit distinctive distributions of CN_{org} that highlight zones of primary framboid growth and subsequent pyrite overgrowths. The pattern of CN_{org} enrichment correlates with pyrite nano-textures showing that organic material is retained at grain boundaries between pyrite micro-crystals and in thin nano-porous rims coating each micro-crystal. Organic material is also found preserved in pyrite overgrowth zones but frequently decreases outwards with progressive overgrowth. The CN_{org} distribution permits accurate measurements of relict framboid versus overgrowth diameters, which is essential if framboids are to be

used as paleo-redox proxies. Our data show that 560 Ma framboids nucleated and grew within organic biofilms, extending geological evidence for this growth mechanism back into the Precambrian. These biofilms also contained sulfate-reducing bacteria, and perhaps also metal reducing bacteria, that provided a local source of reduced S and Fe for the pyrite. Our work provides a straightforward protocol for finding hidden framboids in larger euhedral crystals, and for determining the biogenicity of ancient framboids, enhancing their potential as biomarkers on the early Earth and other planets.

ACKNOWLEDGMENTS

We acknowledge the Australian Microscopy & Microanalysis Research Facility at The University of Western Australia and The University of New South Wales. These facilities are funded by the Universities, State and Commonwealth Governments. DW is funded by the Australian Research Council, via a grant to the Centre of Excellence for Core to Crust Fluid Systems.

REFERENCES CITED

Canfield, D.E., and Thamdrup, B., 1994, The production of ^{34}S-depleted sulphide during bacterial disproportionation of elemental sulfur: Science, v. 266, p. 1973–1975, doi:10.1126/science.11540246.

Canfield, D.E., Poulton, S.W., and Narbonne, G.M., 2007, Late-Neoproterozoic deep-ocean oxygenation and the rise of animal life: Science, v. 315, p. 92–95, doi:10.1126/science.1135013.

Farquhar, J., Cliff, J., Zerkle, A.L., Kamyshny, A., Poulton, S.W., Claire, M., Adams, D., and Harms, B., 2013, Pathways for Neoarchean pyrite formation constrained by mass-independent sulfur isotopes: Proceedings of the National Academy of Sciences USA, v. 110, p. 17638-17643.

Ferris, F.G., Fyfe, W.S., and Beveridge, T.J., 1987, Bacteria as nucleation sites for authigenic minerals in a metal-contaminated lake sediment: Chemical Geology, v. 63, p. 225–232, doi:10.1016/0009-2541(87)90165-3.

Fike, D., Grotzinger, J., Pratt, L., and Summons, R., 2006, Oxidation of the Ediacaran ocean: Nature, v. 444, p. 744–747, doi:10.1038/nature05345.

Flemming, H.-C., 1995, Sorption sites in biofilms: Water Science and Technology, v. 32, p. 27–33, doi:10.1016/0273-1223(96)00004-2.

Hofmann, H.J., O'Brien, S.J., and King, A.F., 2008, Ediacaran biota on Bonavista Peninsula, Nefoundland, Canada: Journal of Paleontology, v. 82, p. 1–36, doi:10.1666/06-087.1.

Kohn, M.J., Riciputi, L.R., Stakes, D., and Orange, D.L., 1998, Sulfur isotope variability in biogenic pyrite: Reflections of heterogenous bacterial colonization?: The American Mineralogist, v. 83, p. 1454–1468.

Large, D.J., Fortey, N.J., Milodowski, A.E., Christy, A.G., and Dodd, J., 2001, Petrographic observations of iron, copper, and zinc sulphides in freshwater canal sediment: Journal of Sedimentary Research, v. 71, p. 61–69, doi:10.1306/052600710061.

Leavitt, W.D., Halevy, I., Bradley, A.S., and Johnston, D.T., 2013, Influence of sulfate reduction rates on the Phanerozoic sulfur isotope record: Proceedings of the National Academy of Sciences of the United States of America, v. 110, p. 11244–11249, doi:10.1073/pnas.1218874110.

Love, L.G., 1957, Micro-organisms and the presence of syngenetic pyrite: Quarterly Journal of the Geological Society of London, v. 113, p. 429–440, doi:10.1144/GSL.JGS.1957.113.01-04.18.

Love, L., and Amstutz, G.C., 1969, Framboidal pyrite from two andesites: Neues

Jahrbuch für Mineralogie, Monatshefte, v. 3, p. 97–108.

MacLean, L.C.W., Tyliszczak, T., Gilbert, P.U.P.A., Zhou, D., Pray, T.J., Onstott, T.C., and Southam, G., 2008, A high-resolution chemical and structural study of framboidal pyrite formed within a low-temperature bacterial biofilm: Geobiology, v. 6, p. 471–480, doi:10.1111/j.1472-4669.2008.00174.x.

McLoughlin, N., Grosch, E.G., Kilburn, M.R, and Wacey, D., 2012, Sulfur isotope evidence for a Paleoarchean subseafloor biosphere, Barberton, South Africa: Geology, v. 40, p. 1031–1034.

Ohfuji, H., and Rickard, D., 2005, Experimental synthesis of framboids – a review: Earth-Science Reviews, v. 71, p. 147–170, doi:10.1016/j.earscirev.2005.02.001.

Ohfuji, H., Boyle, A.P., Prior, D.J., and Rickard, D., 2005, Structure of framboidal pyrite: an electron backscatter diffraction study: American Mineralogist, v. 90, p. 1693–1704.

Papunen, H., 1966, Framboidal texture of the pyritic layer found in a peat bog in S.E. Finland: Comptes Rendus de la Société Géologique de Finlande, v. 38, p. 117–125.

Popa, R., Badescu, A., and Kinkle, B.K., 2004, Pyrite framboids as biomarkers for iron-sulfur systems: Geomicrobiology Journal, v. 21, p. 193–206, doi:10.1080/01490450490275497.

Rickard, D.T., and Zweifel, H., 1975, Genesis of Precambrian sulfide ores, Skellefte district, Sweden: Economic Geology, v. 70, p. 255–274.

Rickard, D., 2012, Sulfidic Sediments and Sedimentary Rocks: Amsterdam, Elsevier, 816 p.

Scott, R.J., Meffre, S., Woodhead, J., Gilbert, S.E., Berry, R.F., and Emsbo, P., 2009, Development of framboidal pyrite during diagenesis, low-grade regional

metamorphism, and hydrothermal alteration: Economic Geology and the Bulletin of the Society of Economic Geologists, v. 104, p. 1143–1168, doi:10.2113/gsecongeo.104.8.1143.

Sweeney, R.E., and Kaplan, I.R., 1973, Pyrite framboid formation: Laboratory synthesis and marine sediments: Economic Geology, v. 68, p. 618–634.

Wacey D., Kilburn, M.R., Saunders, M., Cliff, J., and Brasier, M.D., 2011, Microfossils of sulphur-metabolizing cells in 3.4 billion-year-old rocks of Western Australia: Nature Geoscience, v. 4, p. 698–702.

Wang, L., Shi, X., and Jiang, G., 2012, Pyrite morphology and redox fluctuations recorded in the Ediacaran Doushantuo Formation: Palaeogeography, Palaeoclimatology, Palaeoecology, v. 333–334, p. 218–227, doi:10.1016/j.palaeo.2012.03.033.

Wilkin, R.T., Barnes, H.L., and Brantley, S.L., 1996, The size distribution of framboidal pyrite in modern sediments: An indicator of redox conditions: Geochimica et Cosmochimica Acta, v. 60, p. 3897–3912, doi:10.1016/0016-7037(96)00209-8.

Figure 1. Secondary electron image (SE) and NanoSIMS ion maps of sulfur ($^{34}S^-$), nitrogen ($^{26}CN^-$) and carbon ($^{12}C^-$) showing the internal CN_{org} zoning of 560 Ma pyrite framboids. Two main zones are present: an inner spheroidal zone (ISZ) comprising numerous micro-crystals of pure pyrite set within a matrix of CN_{org}-rich pyrite; and an outer, more homogenous zone (OZ) of CN_{org}-rich pyrite that overgrows the framboids, causing some to be cemented together. Note that neither the sulfur map nor SE image reveal the true structure of the pyrite. NanoSIMS sulfur isotope analysis craters are visible as darker squares in the SE and $^{34}S^-$ images. The black matrix in the SE image is quartz and clay.

Publisher: GSA
Journal: GEOL: Geology
DOI:10.1130/G36048.1

Figure 2. a-c) Modification of framboidal pyrite structure by euhedral overgrowths. Overgrowths on the central row of framboids have subhedral to euhedral crystal form and disguise the true nature of the framboids. White line in (b) shows approximate location of TEM sample analyzed in (d-e). d) Dark-field scanning TEM image of an ultrathin slice (c.100 nm) through a pyrite framboid, highlighting the differences in nano-texture between the inner spheroidal zone (ISZ), nano-porous overgrowth zone (OZ) and outer rim. e) Higher magnification view of the ISZ showing clear nano-porous rims to each pyrite microcrystal (arrows, plus tangential section through the edge of a micro-crystal '1').

Figure 3. Example of sulfur isotope data (δ^{34}S ‰) obtained *in situ* from framboidal pyrite in the c. 560 Ma Fermeuse Formation. These rather homogenous and light δ^{34}S values suggest the source of sulfur for the framboidal pyrite was microbial sulfate reduction under conditions of electron donor limitation.

[1]GSA Data Repository item 2014xxx, xxxxxxxx, is available online at www.geosociety.org/pubs/ft2014.htm, or on request from editing@geosociety.org or Documents Secretary, GSA, P.O. Box 9140, Boulder, CO 80301, USA.

Figure 1
Click here to download high resolution image

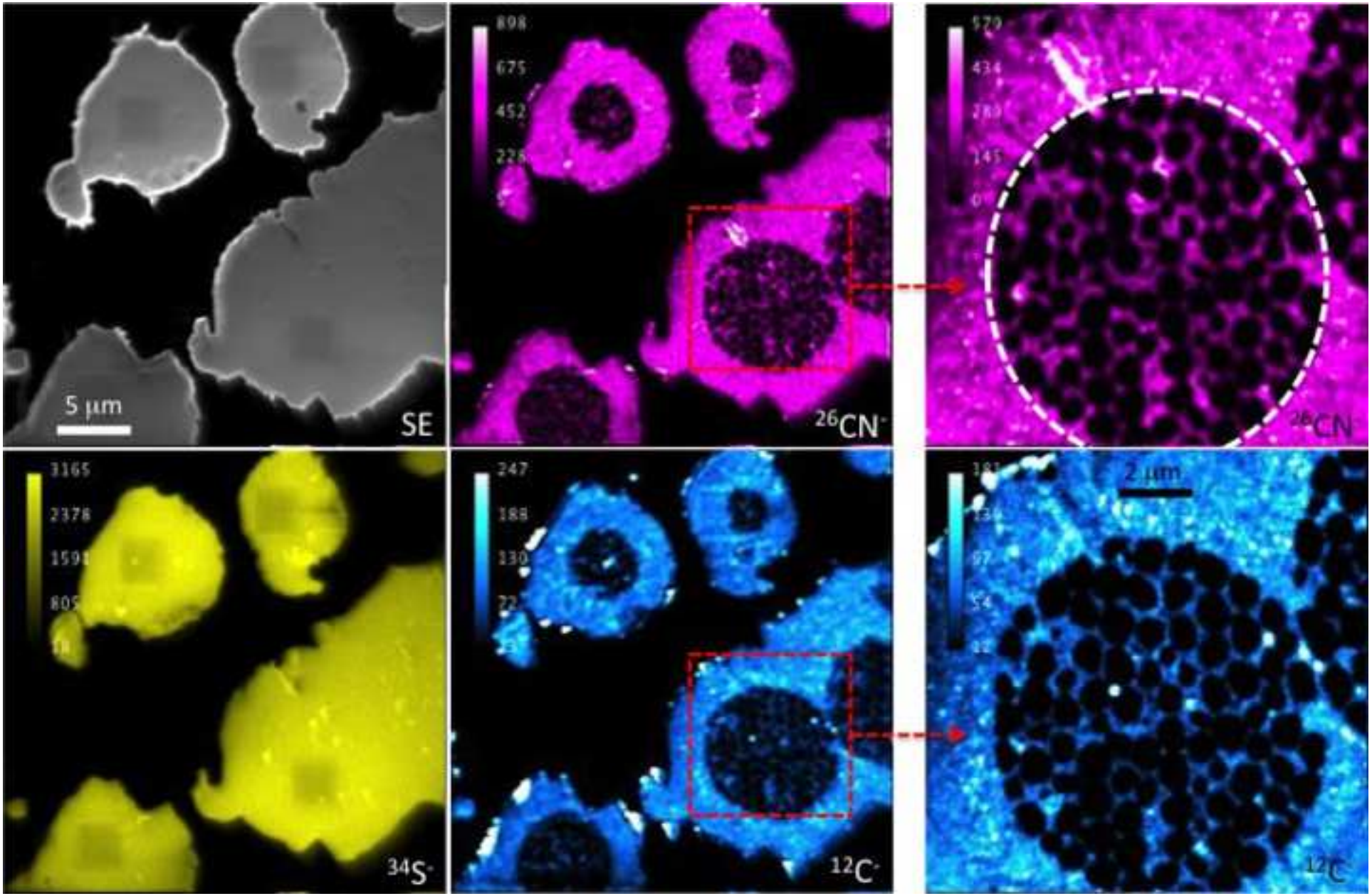

Figure 2
Click here to download high resolution image

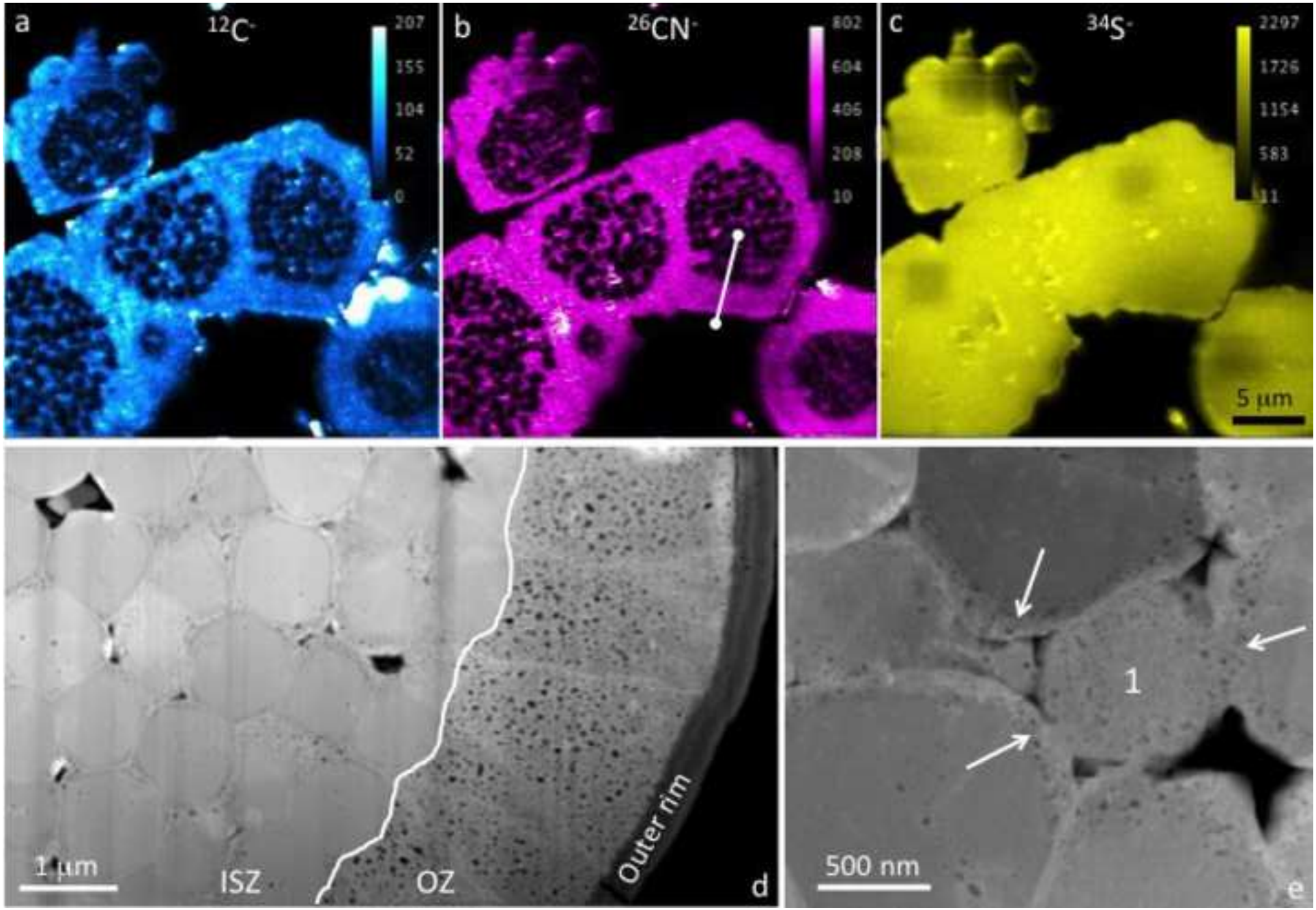

Figure 3
Click here to download high resolution image

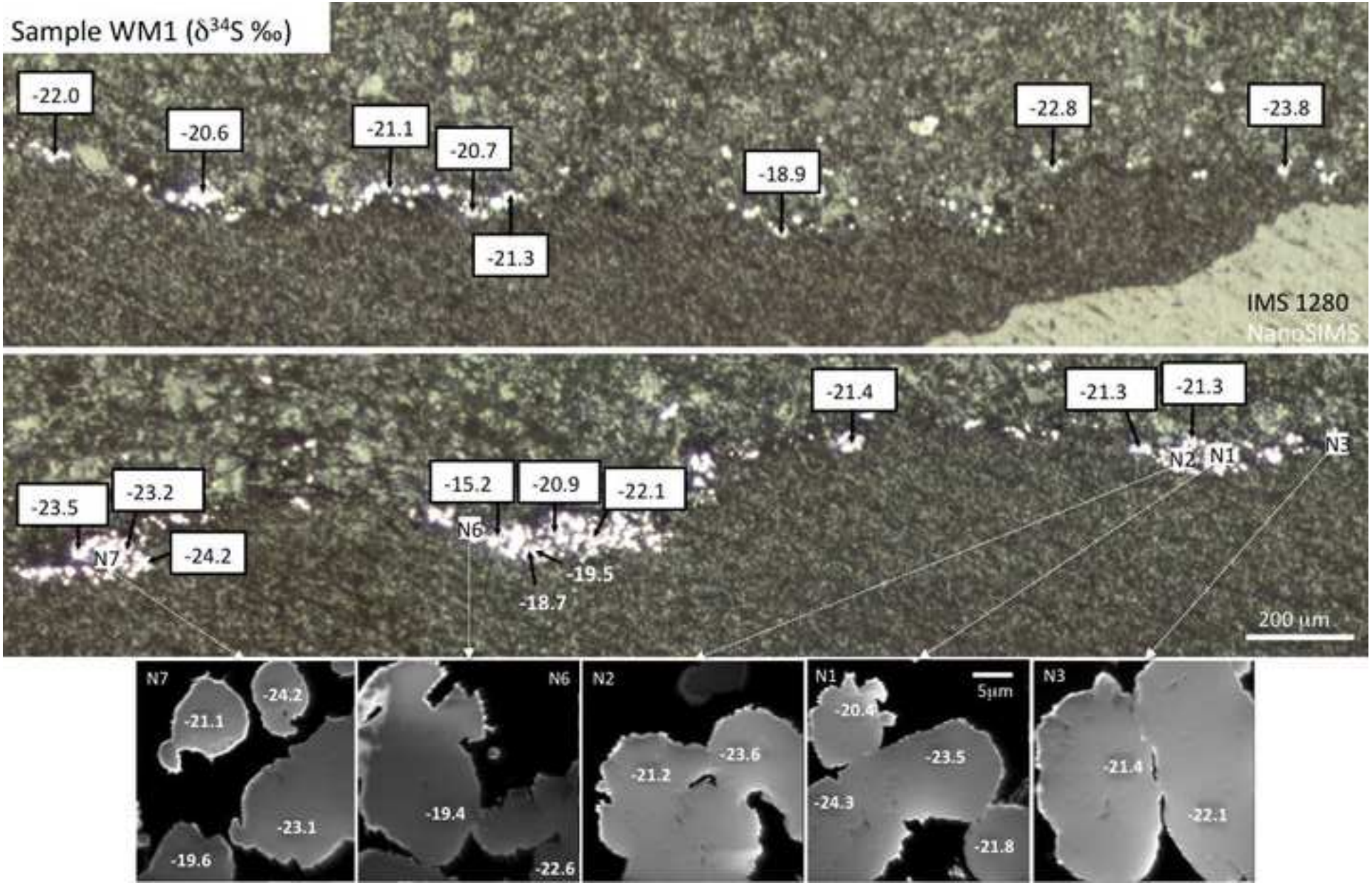

GSA Data Repository Item 2014-XXXX

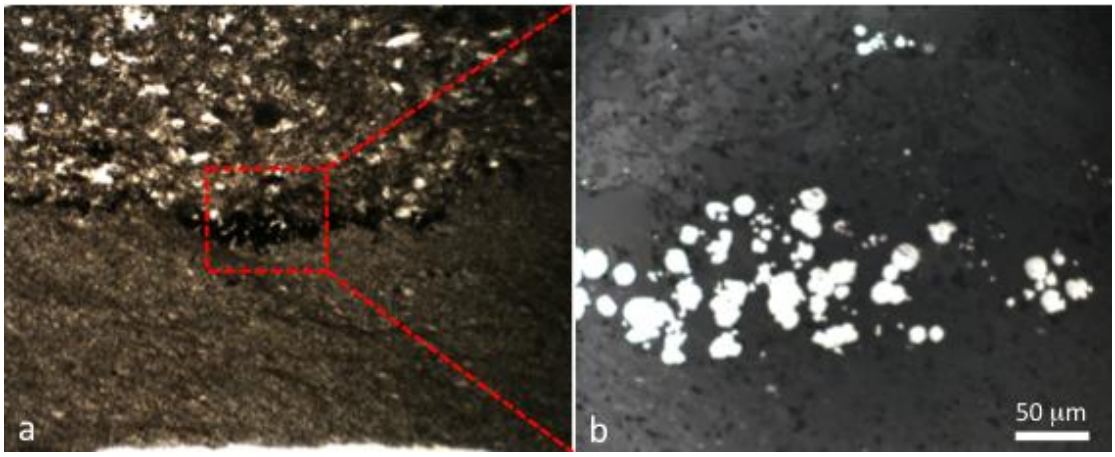

Figure DR1. Occurrence of putative framboidal pyrite from the late Ediacaran of the Catalina Dome, Bonavista Peninsula, Newfoundland (sample WM1, c. 560 Ma Fermeuse Formation). a) Thin section in plane-polarised light showing how framboidal pyrite typically occurs on bedding plane surfaces between a lower mudstone and an upper coarser siltstone or reworked volcanic ash. Impressions of Ediacaran organisms such as *Charniodiscus* sp. and *Bradgatia* sp. are found on this same bedding surface. Note also the wispy carbonaceous laminae that probably represent the remnants of biofilms. b) Higher magnification reflected light image, revealing that the pyrite occurs as both single sub-spherical grains and clusters of cemented and overgrown grains.

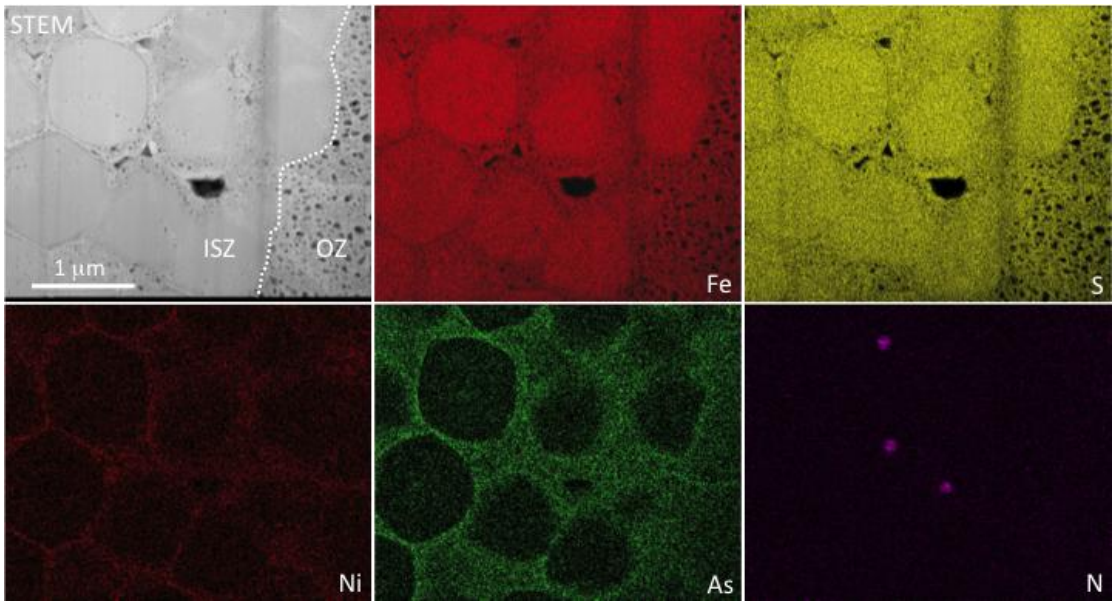

Figure DR2. Dark-field scanning transmission electron microscope (STEM) image, plus ChemiSTEM maps of part of a pyrite framboid (brighter colours indicate higher concentrations of each element). Arsenic and nickel are enriched in the nano-porous rims of the pyrite microcrystals in the ISZ, and also to a lesser extent in the OZ. Nitrogen is seen at some triple junctions in the ISZ, reinforcing our NanoSIMS data. However, the overall pattern of N enrichment seen in NanoSIMS maps is not visible here. This is due to the extreme thinness of the TEM sample and the poorer detection limits for N in the TEM.

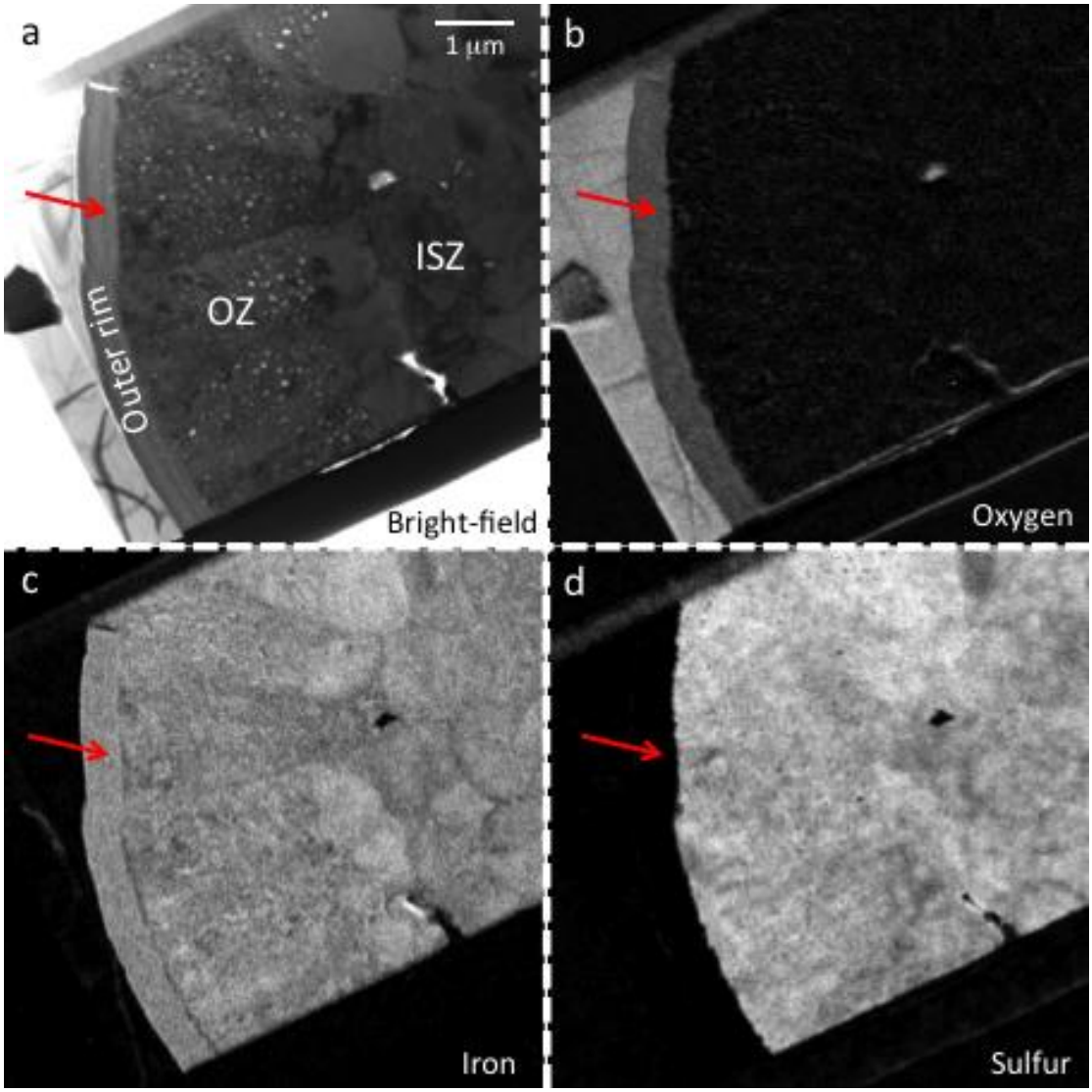

Figure DR3. Bright-field TEM image and energy-filtered (EFTEM) elemental maps from the outer part of a pyrite grain. While the ISZ and OZ are clearly composed of pyrite, the outer rim contains no sulfur and has been oxidised to iron oxide (arrow). The mineral to the left of the iron oxide rim is silica, hence the high oxygen signal.

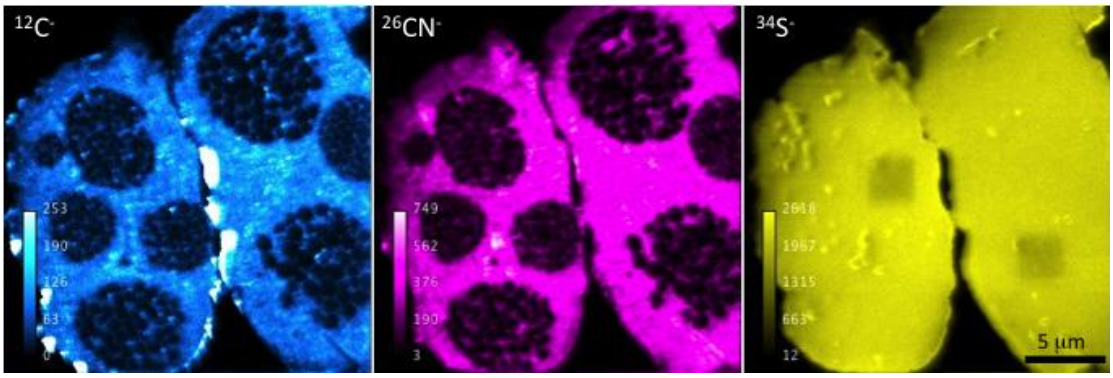

Figure DR4. NanoSIMS ion maps of carbon ($^{12}C^-$), nitrogen ($^{26}CN^-$) and sulfur ($^{34}S^-$) showing organic-rich pyrite overgrowth and cementation of numerous individual framboids. Note that this nano-structure is only visible in the C and CN images.

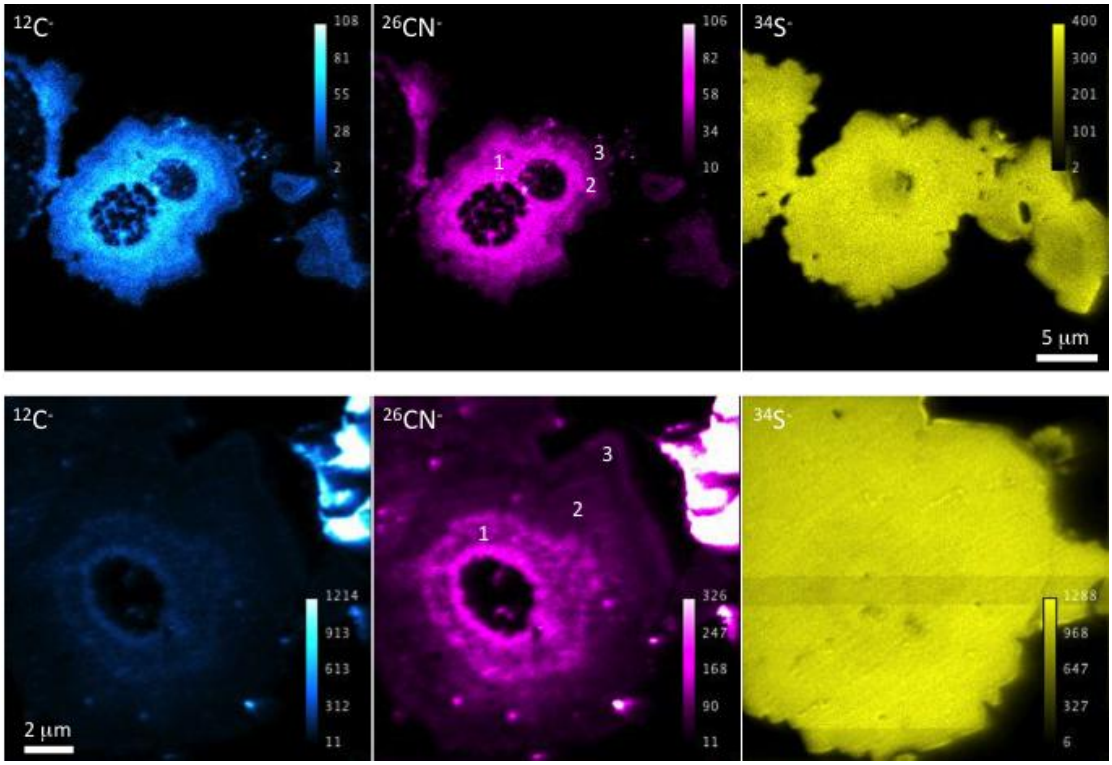

Figure DR5. Examples of concentric zoning of organic material in pyrite framboid overgrowths. Pyrite closest to the original framboids shows the highest concentration of organic material (1). Two further zones (2 and 3) record decreasing concentrations of organic material as the pyrite overgrowth increases in size. Note that sulfur signal is rather uniform across all zones.

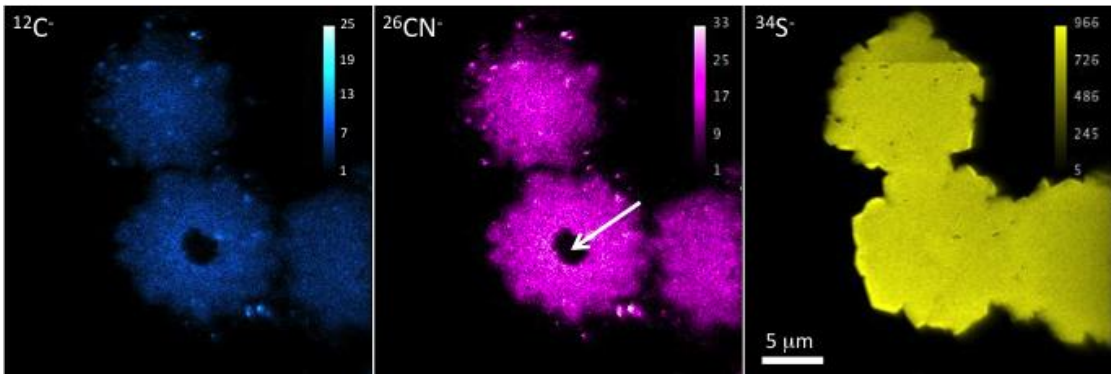

Figure DR6. NanoSIMS ion maps of carbon ($^{12}C^-$), nitrogen ($^{26}CN^-$) and sulfur ($^{34}S^-$) showing more poorly preserved pyrite framboids. The internal zone of micro-grains in an organic matrix is not preserved, being replaced by either a spheroidal pure pyrite core (arrow) or in other cases homogenous organic-rich pyrite.

Table DR1. Sulfur isotope data ($\delta^{34}S_{V\text{-}CDT}$ ‰) from framboidal pyrite within the c. 560 Ma Fermeuse formation of Newfoundland (sample WM1).

Analysis ID	^{34}S counts	$\delta^{34}S_{V\text{-}CDT}$	±2σ (‰)
	SESSION 1 (NANOSIMS)		
Standards	**(x10^6)**		
SON-3_1	5.42	1.8	1.1
SON-3_2	5.24	1.4	0.9
SON-3_3	5.24	2.4	0.9
SON-3_4	5.23	0.6	0.9
SON-3_5	5.18	2.3	1.0
SON-3_6	5.20	3.0	1.0
SON-3_7	5.19	-0.4	1.0
SON-3_8	5.18	1.8	1.1
SON-3_9	5.23	1.2	1.4
SON-3_10	5.12	1.1	1.5
SON-3_11	5.09	2.6	1.5
		Mean = 1.6	
		S.D. = 1.0	
Sample WM1			
WM_1a	4.75	-21.8	0.9
WM_1b	5.31	-23.5	0.8
WM_1c	5.13	-20.4	0.8
WM_2a	4.95	-23.6	0.9
WM_2b	4.95	-21.2	0.9
WM_3a	5.00	-22.1	0.9
WM_3b	4.82	-21.4	0.9
WM_5a	4.21	-18.7	1.0
WM_5b	4.71	-19.5	1.0
WM_6a	4.96	-19.4	1.1
WM_6b	4.97	-22.6	1.1
WM_7a	5.46	-21.1	1.2
WM_7b	5.13	-24.2	1.2
WM_7c	5.01	-23.1	1.3
WM_7d	5.13	-19.6	1.3
WM_1d	5.12	-24.3	1.4
	SESSION 2 (IMS 1280)		
Standards	**(x10^{10})**		
SON-3_1	1.99	1.57	0.06
SON-3_2	1.98	1.57	0.06
SON-3_3	1.99	1.66	0.06
SON-3_4	1.99	1.58	0.06
SON-3_5	2.02	1.60	0.06
SON-3_6	2.07	1.67	0.05
SON-3_7	2.07	1.60	0.05
SON-3_8	2.09	1.66	0.05
SON-3_9	2.07	1.61	0.05
SON-3_10	2.11	1.63	0.05
SON-3_11	2.11	1.65	0.06
SON-3_12	2.11	1.66	0.06

SON-3_13	2.11	1.56	0.06
SON-3_14	2.11	1.55	0.06
SON-3_15	2.13	1.58	0.06
		Mean = 1.61	
		SD = 0.04	
FREO_1	1.96	-4.49	0.05
FREO_2	2.05	-4.40	0.05
FREO_3	2.07	-4.44	0.06
		Mean = -4.45	
		SD = 0.05	
Sample WM1			
WM_1	1.47	-23.48	0.08
WM_2	0.81	-23.15	0.08
WM_3	0.86	-24.23	0.10
WM_4	1.12	-15.21	0.07
WM_5	0.58	-20.90	0.07
WM_6	0.92	-22.12	0.06
WM_7	0.92	-21.42	0.15
WM_8	1.35	-21.29	0.08
WM_9	1.12	-21.33	0.11
WM_10	1.06	-21.26	0.10
WM_11	0.40	-20.71	0.16
WM_12	0.65	-21.13	0.12
WM_13	1.33	-20.60	0.08
WM_14	1.15	-22.00	0.06
WM_15	0.65	-18.85	0.12
WM_16	0.40	-22.76	0.09
WM_17	0.50	-23.75	0.17

Methods

Focussed ion beam (FIB) preparation of TEM samples

A dual-beam FIB system (FEI Nova NanoLab) at the Electron Microscopy Unit, University of New South Wales was used to prepare pyrite framboid TEM samples from standard uncovered polished geological thin sections coated with c.30 nm of gold. Electron beam imaging was used to identify framboids of interest in the polished thin sections allowing site-specific TEM samples to be prepared. The TEM sections were prepared by a series of steps involving different beam energies and currents (see Wacey et al., 2012), resulting in ultrathin wafers of c. 100 nm thickness. These TEM wafers were extracted using an ex-situ micromanipulator and deposited on continuous-carbon copper TEM grids. FIB preparation of TEM sections allows

features below the surface of the thin sections to be targeted, thus eliminating the risk of surface contamination producing artefacts.

TEM analysis of FIB-milled wafers

TEM data were obtained using a *FEI Titan G2 80-200* TEM/STEM with *ChemiSTEM Technology* operating at 200 kV, plus a *JEOL 2100* LaB_6 TEM operating at 200 kV equipped with a *Gatan Orius* CCD camera and *Tridiem* energy filter. Both instruments are located in the Centre for Microscopy, Characterisation and Analysis (CMCA) at The University of Western Australia. HAADF (high angle annular dark-field) STEM images and EDS (*ChemiSTEM*) maps were obtained on the *FEI Titan*. Energy filtered (EFTEM) elemental maps were obtained on the *JEOL 2100* using the conventional three-window technique (Brydson, 2001), with energy windows selected to provide optimum signal-to-noise.

NanoSIMS ion mapping

Ion mapping was performed using a CAMECA NanoSIMS 50 at CMCA, The University of Western Australia, with instrument parameters optimized as described in Wacey et al. (2011). Analysis areas varied from 12 x 12 μm up to 30 x 30 μm, at a resolution of 256 x 256 pixels (each pixel measuring between 47 nm and 117 nm, depending on the image area), with a dwell time of 20 ms per pixel, and a primary beam current of c.2.5 pA. Secondary ions mapped were $^{12}C^-$, $^{26}CN^-$, and $^{34}S^-$ (note the use of $^{34}S^-$ instead of $^{32}S^-$, because $^{32}S^-$ provided too many counts to the electron multiplier detector at the conditions required for good $^{12}C^-$ and $^{26}CN^-$ imaging), and charge compensation was achieved by using the electron flood gun.

NanoSIMS sulfur isotope analysis

Sulfur isotope ratios ($^{34}S/^{32}S$) from individual pyrite grains were determined using a CAMECA NanoSIMS 50 at CMCA, The University of Western Australia. The analyses were performed using a Faraday Cup (FC) detector for the ^{32}S signal and an electron multiplier (EM) for the ^{34}S signal, with a primary beam current of c.2.5 pA, and a raster area of 3 x 3 μm. Instrument setup, data acquisition, drift correction, instrumental mass fractionation correction and error propagation were carried out according to the protocol described in McLoughlin et al. (2012). All samples were confirmed as pyrite using laser Raman spectroscopy, so no corrections for matrix effects between the samples and our SON-3 pyrite standard were applied. Analyses were completed over a single analytical session with an uncertainty on bracketing $\delta^{34}S$ standard analyses of 1.0 ‰ (1SD; n = 11). Propagated errors for individual analyses (2σ) are listed in the final column of Table DR1.

IMS 1280 sulfur isotope analysis

Instrument setup

Sulfur isotope ratios ($^{34}S/^{32}S$) were determined using a CAMECA IMS 1280 ion microprobe operating in multi-collection mode at CMCA, The University of Western Australia. In all cases NMR regulation was used and ^{32}S and ^{34}S were measured using Faraday cup detectors (FC). A rastered beam approach employing dynamic transfer was used. A 3.5 nA focused primary beam was used to pre-sputter the analysis area using a 30 μm × 30 μm beam for 40 seconds followed by automated secondary centering in the field aperture (FA) and entrance slit (ES); and analysis using a 20 μm × 20 μm raster employing dynamic transfer for 45 × 4 second integrations. Unknowns were bracketed with standards of known composition. Other

conditions include a 133 × magnification between sample stage and field aperture (FA), 70 µm entrance slit, 4000 µm FA, 400 µm contrast aperture, a 40 eV energy window with a 5 eV offset to the high energy side, and 500 µm exit slits. Although the pyrite targets are conductors, the normal incidence electron flood gun was utilized for charge compensation in the event that the primary ion beam overlapped onto insulating matrix silica minerals. External precision of $^{34}S/^{32}S$ on the SON-3 standard for the analytical session was better than 0.05 ‰ (1 SD; n = 15). A secondary standard (FREO) was run as an unknown in some cases. These samples returned a mean value of -4.45 ± 0.05 ‰ (1 SD, n = 3), which is in good agreement with the laser fluorination value of -4.3 ‰. Sample count rates varied between ~20 % and 75 % of the count rate of the standard, however, there was no observed correlation between secondary count rate and $\delta^{34}S$ of the samples.

Data processing

Instrumental mass fractionation and propagation of uncertainty follow the protocol in Farquhar et al. (2013). Uncertainty terms included internal uncertainty, external uncertainty of the instrumental mass fractionation of the primary standard, and uncertainty of the standard relative to V-CDT.

References for repository items

Brydson, R., 2001, *Electron Energy Loss Spectroscopy*: Springer-Verlag, New York.

Farquhar, J., Cliff, J., Zerkle, A.L., Kamyshny, A., Poulton, S.W., Claire, M., Adams, D., and Harms, B., 2013, Pathways for Neoarchean pyrite formation constrained by mass-independent sulfur isotopes: Proceedings of the National Academy of Sciences USA, v. 110, p. 17638-17643.

McLoughlin, N., Grosch, E.G., Kilburn, M.R, and Wacey, D., 2012, Sulfur isotope evidence for a Paleoarchean subseafloor biosphere, Barberton, South Africa: Geology, v. 40, p. 1031–1034.

Sim, M.S., Bosak, T., and Ono, S., 2011, Large sulfur isotope fractionation does not require disproportionation: Science, v. 333, p. 74–77.

Wacey D., Kilburn, M.R., Saunders, M., Cliff, J., and Brasier, M.D., 2011, Microfossils of sulphur-metabolizing cells in 3.4 billion-year-old rocks of Western Australia: Nature Geoscience, v. 4, p. 698–702.

Wacey, D., Menon, S., Green, L., Gerstmann, D., Kong, C., McLoughlin, N., Saunders, M., and Brasier, M.D., 2012, Taphonomy of very ancient microfossils from the ~3400 Ma Strelley Pool Formation and ~1900 Ma Gunflint Formation: new insights using focused ion beam: Precambrian Research, v. 220-221, p. 234–250.